Cirrus Clouds and the Large-Scale Atmospheric State: Relationships Revealed by Six Years of Ground-Based Data

GERALD G. MACE, SALLY BENSON, AND ERIK VERNON

Department of Meteorology, University of Utah, Salt Lake City, Utah

(Manuscript received 26 April 2005, in final form 27 October 2005)

ABSTRACT

The properties of cirrus clouds observed at the Atmospheric Radiation Measurement (ARM) Climate Research Facility (ACRF) in Oklahoma are documented from a nearly continuous 6-yr record of 35-GHz cloud radar data. Cirrus frequency over the ACRF is 23% and 28% of the time in the warm (May–September) and cold seasons (November–March), respectively, with maxima and minima during the period studied of 30% and 16% in the warm season and 34% and 24% in the cold seasons. Cirrus, as defined here, reveal a seasonal oscillation in their macroscale properties that can be traced to the seasonal deepening of the troposphere in the Southern Plains region. While the average bulk microphysical properties do not change significantly from season to season, the variability of certain parameters demonstrates seasonal change. It is shown that the properties of cirrus clouds vary perceptively with the large-scale vertical motion. Using NCEP–NCAR reanalysis data to define the large-scale meteorological state when cirrus are observed at the ACRF, the authors find that cirrus tend to exist within a maximum in upper-tropospheric humidity and downstream of the peak upper-tropospheric vertical motion. Cirrus that exist in large-scale ascent upstream of the synoptic-scale middle-tropospheric ridge axis are shown to have higher water contents than cirrus that exist in large-scale subsidence downstream of the ridge axis, although the overall nature of the statistical distributions of water contents do not change greatly, suggesting that it may be difficult to parameterize the properties of cirrus based solely on large-scale vertical motion. The layer-mean particle size, on the other hand, shows no such sensitivity to the large-scale vertical motion.

1. Introduction

The need to correctly represent cirrus clouds in numerical models of the earth's general circulation (GCMs) is well established (Stephens 2005; Del Genio 2002). Cirrus in the upper troposphere largely regulate the terrestrial radiation emitted to space and also modulate the solar radiation that ultimately penetrates to the surface. The complicated interplay of these competing feedback mechanisms are mitigated to some extent by the typical radiative properties of cirrus that, compared to other climatically important clouds, derive from rather low concentrations of large ice particles resulting in cloud layers that are typically transmissive to solar radiation. The global coverage of cirrus derived from satellite data (Wylie and Menzel 1999) is on the order of 40% with the greatest coverage in the tropical regions, although cirrus of the middle latitudes are significant components of the earth's energy budget also (Heymsfield and McFarquhar 2002). Cirrus, by definition, are semitransparent (Sassen 2002) and have widely varying properties such as water content, particle size, and optical depth (Heymsfield and McFarquhar 2002; Mace et al. 2001; Comstock et al. 2002).

Cirrus are unique in that they can be derived from several source mechanisms. One of the more easily recognized dynamical mechanisms that form cirrus is detrainment from deep convection where the flux of condensate mass spreads from small-scale updrafts. In contrast, cirrus are also formed through the comparatively gentle ascent of air masses associated with middle-latitude weather disturbances (Heymsfield 1977; Lin et al. 2005) and through the generation of local convective instabilities through differential advection that form mesoscale complexes of cirrus uncinus cells (Sassen et al. 1989). These cloud types have been documented in several recent field programs (Gayet et al. 2004; McGill et al. 2004), and they continue to be objects of interest for field studies. However, the development of param-

Corresponding author address: Associate Professor Gerald G. Mace, 201 South 1460 East, Rm. 819 (819 WBB), Dept. of Meteorology, University of Utah, Salt Lake City, UT 84112-0110.
E-mail: mace@met.utah.edu

eterizations unique to upper-tropospheric cloud systems has not advanced, and many outstanding questions remain unanswered from a parameterization standpoint (Del Genio 2002).

With the advent of global models that include condensed water as a prognostic variable, the occurrence of cloud within a grid box is predicted by the source and loss mechanisms associated with condensation and precipitation within the grid box (Del Genio et al. 1996). While prognostic condensed water is a significant step forward from the diagnostic parameterizations of previous generations of models, GCMs predict only the grid box mean mixing ratio of condensate. Parameterizations are still required to determine what fraction of the grid box contains cloud. While particle size is often assumed in GCMs, the cloud fraction parameterization leads also to an effective cloud liquid water content that often determines a sedimentation rate (Heymsfield and Donner 1990) following some autoconversion rate of cloud water to precipitation (Sundqvist 2002). The radiative properties that determine the net heating in cirrus layers is often parameterized using the water content and particle size (Fu and Liou 1993). In most cases the effective particle size is not predicted even though it is important in determining the radiative properties and sedimentation rate in the natural atmosphere.

Critical evaluation of GCM parameterizations can take several approaches. On the one hand, it is clearly necessary that the physical state of the atmosphere must lead, in the end, to energy balance at the top of the atmosphere consistent with observations such as the Earth Radiation Budget Experiment (ERBE; Smith et al. 1994) and Clouds and the Earth's Radiant Energy System (CERES; Wielicki 2001). Another consideration, one that is more subtle, is that the spatial distribution of the predicted radiative feedbacks that drive the general circulation must also be consistent with what occurs within the real atmosphere (Webster and Stephens 1984). Without this internal spatial consistency, there is no guarantee that the predicted climate state, fixed to top-of-the-atmosphere (TOA) radiation measurements, will actually represent the atmosphere: agreement with the TOA radiation balance is a necessary but not a sufficient constraint (Webster and Stephens 1984; Stephens 2005). Therefore, documentation of the relationships between large-scale atmospheric states and the clouds that exist within them is required to establish the validity of GCM predictions. Even though study of these relationships may not themselves result directly in improved parameterizations, they will facilitate, through advancement in our basic knowledge, a realistic and critical assessment of the coupling between the dynamical and physical components of a model.

A reasonably extensive body of work documenting middle-latitude and tropical cirrus microphysical properties exist in the literature (e.g., Heymsfield and McFarquhar 2002, and references therein), and recent efforts such as the Cirrus Regional Study of Tropical Anvils and Cirrus Layers Florida Area Cirrus Experiment (CRYSTAL FACE; Jensen et al. 2004) further extend these findings. However, only a few studies have been published that attempt to document the relationships between cirrus properties and the large-scale environments in which these clouds exist (Heymsfield 1977; Starr and Wylie 1990; Mace et al. 1995). Recently, Stubenrauch et al. (2004) considered the properties of cirrus globally using polar-orbiting satellite data and attempted to relate their derived properties with large-scale atmospheric properties. Our goal here is to further document, using ground-based observations, the relationships between middle-latitude cirrus and their large-scale environments. We use a dataset formed by continuously operating active and passive remote sensors at the Atmospheric Radiation Measurement (ARM; Ackerman and Stokes 2003) Southern Great Plains (SGP) Climate Research Facility (ACRF) site near Lamont, Oklahoma. While the SGP site began collecting data in 1993, a millimeter-wave cloud radar (MMCR; Moran et al. 1998) was added in late 1996. The dataset that we consider begins in 1997 and extends through 2002. To this dataset we add the National Centers for Environmental Prediction–National Center for Atmospheric Research (NCEP–NCAR) reanalysis (Kalnay et al. 1996) to document the state of the large-scale atmosphere. We also use vertical motions diagnosed over the ACRF by the European Centre for Medium-Range Weather Forecasts (ECMWF) model as a consistency check. We present the analysis technique in the next section followed by a description of the relationships found between the presence of cirrus over the SGP site and the meteorological state of the synoptic-scale atmosphere. The retrieved bulk microphysical properties will then be examined in terms of their statistics as a function of season and their sensitivity to the magnitude of the large-scale vertical motion in the upper troposphere.

2. Analysis technique

In two earlier papers (Mace et al. 1997, 2001, hereafter M97 and M01, respectively) we explored an approach to establishing the presence of cirrus using a millimeter-radar reflectivity-based definition and reported on the statistical properties of cirrus derived

from extended datasets. In this paper, we evaluate a 6-yr record of cirrus using the same set of instruments as that used in M01. In that study, the ARM 35-GHz vertically pointing MMCR data are processed using an approach similar to that described by Clothiaux et al. (1999) and Clothiaux et al. (2000) for cloud masking and merging of the four data collection modes of the MMCR. One of the advantages of using a sensitive millimeter radar for the study of cirrus occurrence is the capacity for such instruments to penetrate lower-level clouds and even light precipitation to sense clouds near the tropopause. The MMCR is fully attenuated only during periods of moderate or greater liquid precipitation and, while precipitation is a relatively rare occurrence, we remove from the analysis any periods when precipitation is recorded at the surface. During the 6-yr period, the instrumental characteristics of the MMCR were essentially unchanged and the sensitivity of the radar was stable.

In the earlier studies, we identified cirrus using a reasonably straightforward definition that attempted to isolate layers where cirrus microphysical processes and in situ generation were most likely predominant. In other words, we narrowed our focus to ice cloud layers in the upper troposphere where, excluding outflows from deep convection, nucleation of cirrus ice crystals through homogeneous or heterogeneous nucleation were the likely primary means of formation (Sassen and Dodd 1988; Lin et al. 2005). We required the layers to have cloud tops as observed by radar that extended to temperatures colder than 228 K, have a layer maximum radar reflectivity colder than 253 K, and have a cloud base colder than 273 K. This definition excluded layers where a significant degree of liquid phase was present and effectively excluded the tops of deep or otherwise precipitating frontal layers. This rigid temperature threshold definition was suitable for our purpose when our goal was to simply combine all observations into a single analysis set since it was preferable to err on the side of excluding a small fraction of the observations that might otherwise be classified as cirrus than to include layers that may have biased our results.

In the present work, we attempt also to also examine the properties of cirrus events defined as contiguous 30-min periods where at least 0.75 of all profiles from the MMCR include cirrus. We found that the rigid definition of cirrus used in M01 resulted in many of these periods being separated into multiple events even though the period may have had continuous cloudiness that missed one of the criteria slightly. Figure 1 shows an example. On 23 December 1998 a cirrus layer was observed by the MMCR from the beginning of the UTC day until roughly 1800. During much of this time the layer passed the M01 definition. There were periods, however, when the layer thinned (near 1200 UTC) and the requirements were not met although the layer was more or less continuous. We have, therefore, developed a more flexible empirical approach where the same basic elements as considered by M01 are examined except that the fixed thresholds are relaxed to warmer temperatures (Table 1) and a score is accumulated based on temperature criteria. For a layer to be considered cirrus, a score of 15 must be accumulated according to the expression,

$$P_{\text{total}} = \sum_{i=1}^{3} \frac{10}{T_{2i} - T_{1i}} (x_i - T_{1i}),$$

where x_i is the observed temperature of the ith condition listed in Table 1. Note that with the temperatures in Table 1 the value of a given test is always one-half the temperature difference. Also, any negative value of the expression inside the summation always disqualifies the layer. With this approach we require the temperatures of the layer maximum dBZ_e, the echo top temperature, and the layer base temperatures to be colder than the values T_1 and any layer that just meets a requirement will also have to be somewhat colder than the minimum requirement of one additional criterion for the layer to be considered cirrus. While this approach is clearly ad hoc, it does capture the essential elements of the M01 definition while allowing for flexibility. The results applied to the case shown in Fig. 1 can be examined. Inspection of the MMCR data for the six-year period under consideration confirm that this approach captures most layers that an observer of the data would consider to be cirrus, and there are very few cases where a cirrus layer is excluded or a layer that does not appear to be cirrus is included.

As in M01, we also examine the bulk microphysical properties of cirrus and cirrus events using a multisensor algorithm that combines radar reflectivity and infrared radiances observed by an interferometer (hereafter denoted as the ZR algorithm). This technique was initially described in Mace et al. (1998) and more recently in Mace et al. (2005). The ZR technique for calculating the cirrus layer microphysical properties from the remote sensing data is now well established and has been compared to other algorithm results (Comstock et al. 2002), and validated with aircraft data (Mace et al. 2005). Essentially, the algorithm requires the cirrus layer to be optically thin (visible optical depth less than about 5 and infrared emittance less than approximately 0.85) and have no cloud layers below it. The layer-mean radar reflectivity is combined with the IR emissivity derived from the Atmospheric Radiance Emittance In-

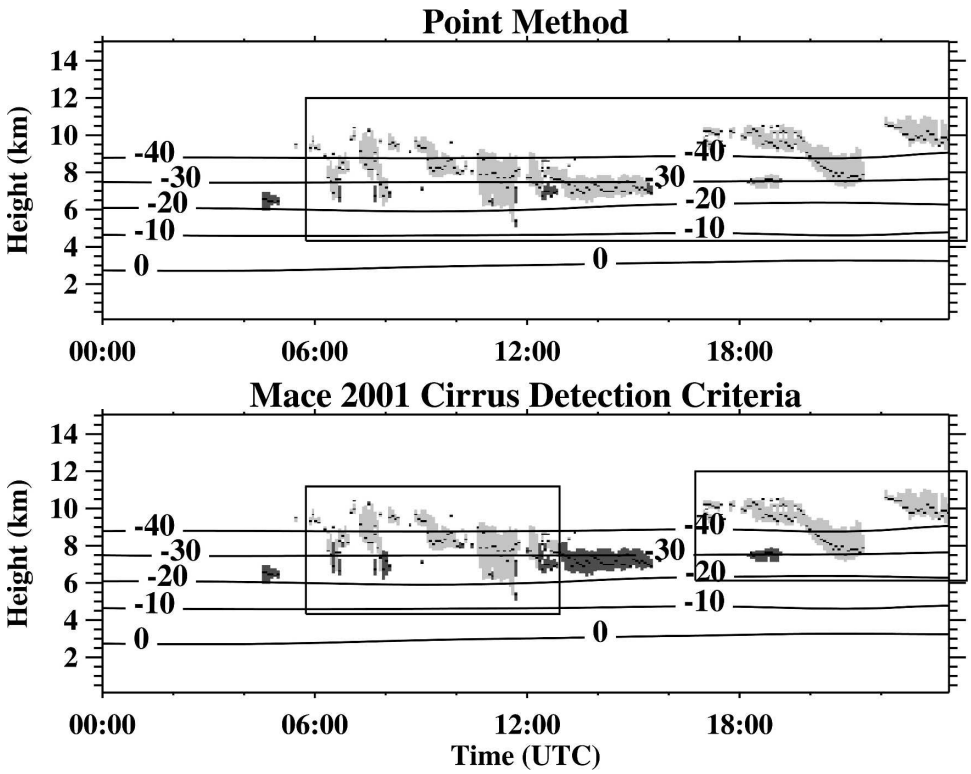

FIG. 1. Example of the effect of the flexible cirrus definition (top) used in this paper compared to that (bottom) used in Mace et al. (2001). The height–time cross section of MMCR radar reflectivity from the SGP ARM site where clouds designated cirrus have a lighter shading than clouds not designated cirrus. Superimposed on the diagrams are temperature contours derived from soundings. The boxes enclose cirrus events using the definition in the text, and the dotted lines in the cirrus layers show the height of maximum radar reflectivity.

terferometer (AERI; Smith et al. 1993) and a first-order gamma distribution of low-density equivalent spheres is found that is simultaneously consistent with the AERI-derived emittance and the layer-mean radar reflectivity. Importantly, the bulk water density of the spheres obeys the size–density relationship found by Brown and Francis (1995). In Mace et al. (2005), we report an extensive in situ validation effort of this algorithm and comparison to satellite cloud property retrievals. We find that that the ice water path (IWP) returned by the ZR algorithm agrees with in situ data to within a root mean square of 20% while the effective radius agrees to in situ data to within a rms of 30%.

TABLE 1. Temperature criteria used in the definition of cirrus layers from the MMCR data.

Temperature of i	T_{1i}	T_{2i}
Max dBZ_e	273	253
Layer top	243	223
Layer base	273	253

Throughout this paper, we will refer to the subset of data to which the ZR algorithm has been applied as the thin cirrus subset (hereafter referred to as ThCi) and compare it to the full dataset (hereafter referred to as AllCi).

Our goal in this paper is to characterize the relationship between cirrus properties and the large-scale atmosphere. In M97 and M01 we used output from the Rapid Update Cycle model, averaged over a 250 × 250 km domain centered on the ACRF, to quantify the large-scale vertical motions from the model-diagnosed divergence profiles. In the present work, the state of the large-scale atmosphere is derived primarily from the NCEP–NCAR reanalysis data (Kalnay et al. 1996; Kistler et al. 2001). The NCEP–NCAR reanalysis data that we use contains dynamic and thermodynamic variables on a 2.5° latitude–longitude grid at 17 pressure levels. These variables are valid at 0000, 0600, 1200, and 1800 UTC of each day. We examine the large-scale ascent, the relative humidity at the 300-hPa level, and the 500-hPa heights, absolute vorticity, and wind. When

deriving statistics and meteorological anomalies during cirrus events, we find the nearest NCEP analysis time to the cirrus observation in question and associate that synoptic-scale environment to the cirrus observations. While we are appropriately skeptical of the absolute values of certain quantities in the NCEP–NCAR reanalysis data, such as vertical motion and humidity in the upper troposphere, our analysis goals can be addressed by examining how cirrus occurrence and properties are related to patterns in the large-scale atmosphere from which we attempt to infer qualitatively the relationships between the clouds and their environment. To place the meteorological patterns into a seasonal context, we examine the regional meteorological anomalies of quantities during periods when cirrus were observed by the MMCR compared to the 30-yr-averaged seasonal mean state. We also consider output from the ECMWF model.

To establish the statistical significance of a large-scale dynamical quantity, we estimate the likelihood that the mean of that quantity at a geographical point sampled during the occurrence of cirrus at the ACRF is similar to a random sampling of that quantity's climatological distribution and not due to systematic differences in the meteorology during cirrus events, that is, a null hyopthesis. Using the z score (Spatz 1997), $z = (\overline{X} - \mu)/\sigma_{\overline{X}}$, we determine how many standard errors the distribution of a quantity with mean $\overline{X}$ and standard error $\sigma_{\overline{X}}$ are from the overall population mean, μ when the tested distribution is created when cirrus are observed at the ACRF. In the case of the anomalies, $\mu = 0$. Statistical significance is then represented as the 95% likelihood ($z > 2$) that the distribution sampled when cirrus are observed at the ACRF cirrus is not drawn randomly from the climatological distribution.

3. Cirrus occurrence

The cirrus occurrence statistics for the 6-yr period are shown in Fig. 2 and summarized in Tables 2 and 3. Figure 3 shows a composite annual cycle of the time series shown in Fig. 2. Overall, cirrus are found to occur 25% of time over north-central Oklahoma with 37% of those cirrus occurring above lower-level cloud layers. In their most recent analysis, Wylie and Menzel (1999) find using the CO_2 slicing method applied to High-Resolution Infrared Radiation Sounder (HIRS) data that cirrus occur between 30% and 40% of the time in this region. While we find considerable variability in the annual cycle of cirrus occurrence, there does seem to be a bimodal cycle that peaks in midwinter with the intensity of polar and subtropical jet maxima over this region and again in midspring as the decreasing frequency of occurrence of middle-latitude storms overlaps with the increasing frequency of convective events in this region. An exception to this tendency can be seen in spring 1998 when the occurrence frequency remained low through the spring and into the summer months. Cirrus tend to be least frequent in late summer and early autumn as the upper troposphere dries in the stable descending air associated with the subtropical high pressure that is typically persistent over this region in late summer. The cirrus that are observed during late summer are often associated with the remnants of tropical systems that move over the ARM site from the western Gulf of Mexico and also from the eastern Pacific. The case study recently described by Sassen et al. (2003) documented such an event over the ACRF that was sampled by aircraft during September 1997. The occurrence of cirrus above low-level clouds is found to be a minimum in late summer. While most years show this pattern, it is especially well defined during 1997.

A strong annual cycle is found in the base, top, and midcloud heights although the layer thickness and cirrus temperature show little discernable seasonal trends. The cycle in cirrus height tends to follow the seasonal tropopause height changes as derived from radiosonde data collected at the ACRF. It is interesting to note that the decrease in cirrus heights seems to be more abrupt and occurs sooner than the decrease in tropopause heights during the latter half of the year. For instance, in 1997, the cirrus top height peaked in July and decreased abruptly in September when the occurrence frequency also decreased. The trend in top height was then a slow decrease throughout the winter and an abrupt increase in March 1998.

In Fig. 2f we show the 6-yr time series of the monthly mean radar reflectivity factor ($\overline{Z}_e$) presented in dB units. This quantity was compiled by averaging the individual values of Z_e in the radar range bins of cirrus layers. Since the radar reflectivity varies naturally in a logarithmic fashion covering three orders of magnitude in typical cirrus, this averaged quantity needs to be interpreted carefully since it is determined inordinately by the larger values. With that in mind, we do find an interesting annual cycle in $\overline{Z}_e$. Minimum values in $\overline{Z}_e$ are typically found during the winter seasons and seem to rise consistently into midsummer. This tendency is fairly robust in all years except 2000 when the $\overline{Z}_e$ seemed to remain below the seasonal mean value. The overall trend identified here suggests that high values of radar reflectivity and the occurrence of volumes with large particles and high values of ice content occur preferentially during the warm season. This tendency is likely associated with an increased frequency of thunderstorm anvil cirrus. Also, owing to the nonlinear character of the radar reflectivity, it is important to

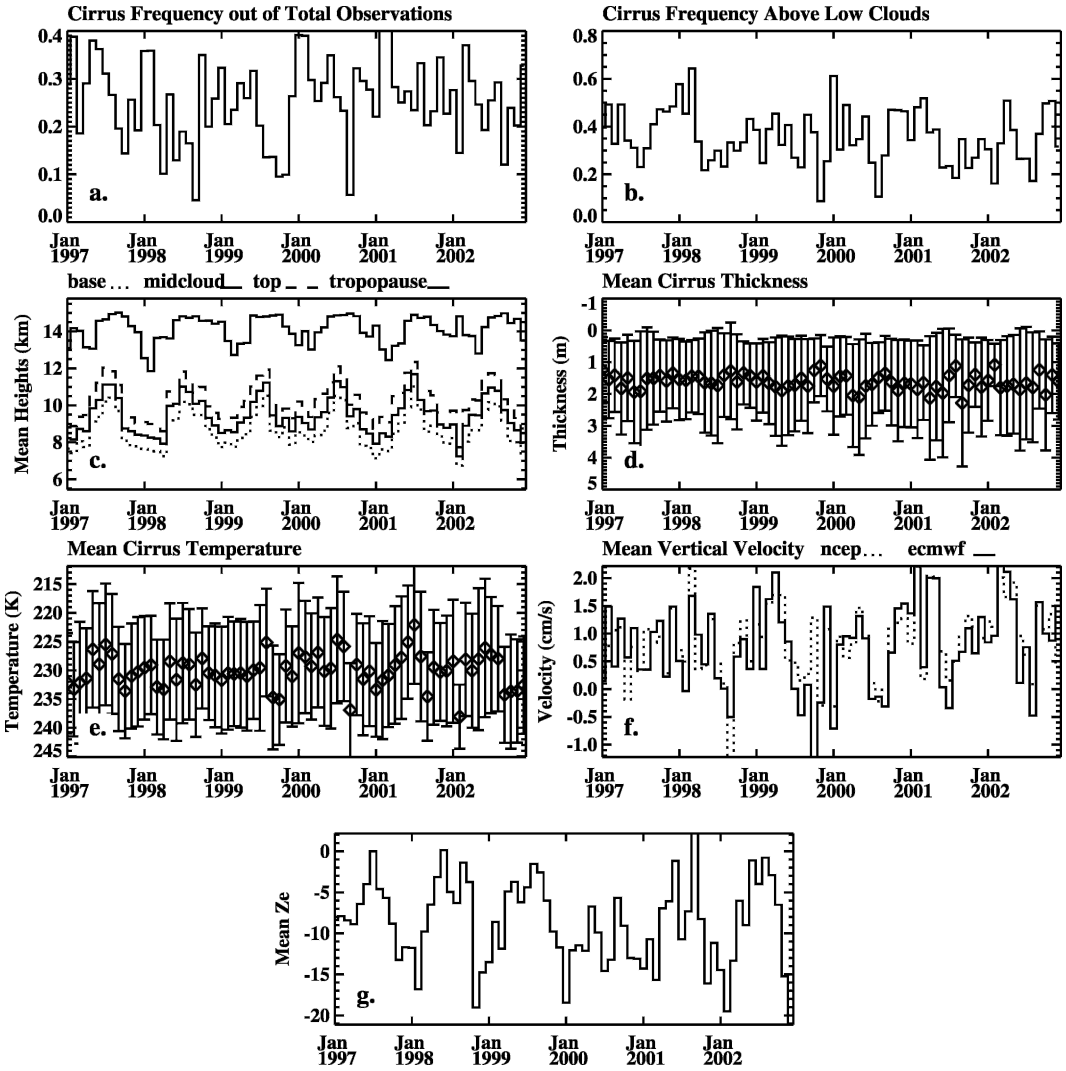

FIG. 2. Monthly mean cirrus statistics during the study period: (a) Frequency of occurrence of all cirrus, (b) fraction of cirrus that occur coincidently with lower-level clouds, (c) layer locations and cold point tropopause heights, (d) mean layer thickness and standard deviation, (e) mean and standard deviation of temperature, (f) mean vertical motion from NCEP (dashed) and ECMWF (solid) during cirrus events, and (g) mean radar reflectivity factor (Z_e) expressed in dBZ_e.

realize that the increase may also be due to an increased frequency of warmer or thicker layers that may not show up statistically in Fig. 2d or Fig. 2e.

In Table 3, we compare the height and temperature statistics of ThCi with similar statistics reported by Sassen and Campbell (2001) that were derived using lidar observations over Salt Lake City, Utah. Comparing the statistics from these two datasets is reasonable because the restrictions to lidar observations of cirrus are similar to the restrictions associated with the ZR algorithm. We find reasonable agreement between the statistics of ThCi and the lidar dataset collected over northern Utah with the exception of the cloud layer thickness and base height. Since millimeter cloud radars are known to be much less sensitive to small particles compared to optical lidar systems, one would expect a bias in the cloud boundaries to occur in the top heights. The mean layer top heights and mean temperatures are, however, nearly identical in the two datasets. While an explanation for this difference may be related to local differences (e.g., the Utah data include summertime outflows from weak monsoonal convection), in any case, the comparison lends credence to the temperature-based definition that we have adopted since the lidar dataset was based on identification of cirrus occurrence strictly by visual appearance of the cloud layers and was natu-

TABLE 2. Cirrus occurrence statistics derived using the definition in the text applied to MMCR data collected at the ACRF from 1997 to 2002. The first row shows the fraction of the time cirrus were observed and the second row shows the fraction of the occurrence that cirrus in the first row were found above lower-level clouds. The following rows show the mean and standard deviation as the first number in each table cell with the median as the second number and the mode of the distribution as the third number. The periods NDJFM and MJJAS represent the cold (November–March) and warm (May–September) seasons, respectively.

	Annual	NDJFM	MJJAS	DJF	MAM	JJA	SON
Cirrus frequency	0.25	0.28	0.23	0.30	0.27	0.25	0.19
Cirrus frequency above low clouds	0.37	0.42	0.30	0.42	0.40	0.27	0.38
Base (km)	8.60 ± 1.97	7.84 ± 1.71	9.56 ± 1.92	7.76 ± 1.74	8.31 ± 1.82	9.96 ± 1.89	8.58 ± 1.71
	8.65	7.84	9.73	7.76	8.39	10.10	8.74
	9.10	7.30	10.00	7.30	8.20	10.00	9.10
Top (km)	10.17 ± 1.62	9.31 ± 1.35	11.20 ± 1.42	9.24 ± 1.38	9.96 ± 1.44	11.57 ± 1.34	10.11 ± 1.34
	10.19	9.38	11.27	9.28	10.01	11.62	10.19
	10.90	9.10	11.80	9.10	10.00	11.80	10.90
Mid-cloud height (km)	9.38 ± 1.65	8.57 ± 1.40	10.38 ± 1.48	8.50 ± 1.43	9.14 ± 1.45	10.77 ± 1.42	9.34 ± 1.38
	9.38	8.52	10.36	8.43	9.10	10.77	9.38
	9.60	8.20	10.40	8.20	8.60	11.30	9.10
Layer thickness (km)	1.66 ± 1.47	1.57 ± 1.27	1.72 ± 1.64	1.57 ± 1.28	1.74 ± 1.52	1.71 ± 1.63	1.62 ± 1.42
	1.17	1.17	1.17	1.17	1.26	1.17	1.17
	0.18	0.18	0.18	0.18	0.18	0.18	0.18
Temperature (K)	229.77 ± 9.93	230.70 ± 9.47	228.44 ± 10.46	230.71 ± 9.58	229.63 ± 9.90	227.47 ± 10.47	231.49 ± 9.23
	230.05	231.14	228.46	231.12	230.04	227.22	231.53
	230.00	234.00	225.00	234.00	233.00	222.00	230.00
Layer top–tropopausedistance	−3.78 ± 2.05	−4.25 ± 2.28	−3.21 ± 1.60	−4.29 ± 2.34	−3.38 ± 2.13	−3.17 ± 1.46	−4.42 ± 1.67
	−3.69	−4.41	−3.15	−4.41	−3.15	−3.15	−4.50
	−3.70	−6.40	−3.70	06.40	−1.90	−2.70	−4.60
dBZ_e	−24.84 ± 12.18	−25.61 ± 11.48	−24.42 ± 13.02	−25.38 ± 11.90	−24.89 ± 12.01	−25.15 ± 13.21	−23.57 ± 11.39
	−26.01	−26.08	−26.46	−25.79	−25.89	−27.47	−24.88
	−26.60	−29.00	−32.50	−28.70	−27.80	−34.70	−28.20
ECMWF vertical motion (cm s^{-1})	0.89 ± 2.84	0.99 ± 2.87	0.60 ± 2.52	1.01 ± 2.91	1.31 ± 3.40	0.35 ± 2.07	0.76 ± 2.48
	0.40	0.60	0.16	0.62	0.60	0.04	0.45
	−0.20	0.70	−0.20	0.60	0.10	−0.20	−0.10
NCEP vertical motion (cm s^{-1})	0.89 ± 2.25	0.92 ± 2.38	0.71 ± 1.95	0.87 ± 2.38	1.21 ± 2.56	0.52 ± 1.70	0.92 ± 2.06
	0.68	0.79	0.47	0.79	0.94	0.31	0.78
	0.20	1.00	0.30	0.90	−0.10	−0.20	0.10
Z_e	−6.49 ± 2.25	−12.13 ± −3.53	−3.70 ± 4.03	−11.81 ± −3.73	−7.23 ± 1.41	−3.68 ± 3.94	−5.84 ± 2.96
	−26.01	−26.08	−26.46	−25.79	−25.89	−27.47	−24.88
	−43.01	−43.01	−40.97	−43.01	−43.01	−40.97	−42.22

TABLE 3. As in Table 2, except that the thin cirrus subset is shown and results from Sassen and Campbell (2001) are listed. Since it is not relevant, we excluded the row for the frequency of cirrus above lower-level clouds.

	Sassen and Campbell (2001)	Annual	NDJFM	MJJAS	DJF	MAM	JJA	SON
Frequency of all cirrus								
Base (km)	8.2 ± 1.7	9.40 ± 1.83	8.48 ± 1.60	10.35 ± 1.62	8.42 ± 1.64	8.90 ± 1.62	10.69 ± 1.56	9.18 ± 1.50
		9.47	8.52	10.39	8.45	8.95	10.78	9.34
		9.90	5.00	10.90	5.00	9.10	10.90	9.60
Top (km)	11.0 ± 1.7	10.80 ± 1.77	9.94 ± 1.54	11.71 ± 1.54	9.89 ± 1.62	10.27 ± 1.57	12.08 ± 1.45	10.53 ± 1.43
		10.87	10.12	11.85	10.06	10.33	12.26	10.71
		10.80	10.80	12.20	10.80	10.20	12.20	10.80
Mid-cloud height (km)	9.6 ± 1.7	10.10 ± 1.74	9.21 ± 1.51	11.03 ± 1.51	9.15 ± 1.57	9.59 ± 1.53	11.38 ± 1.42	9.85 ± 1.40
		10.18	9.32	11.11	9.24	9.66	11.50	10.01
		10.50	8.70	11.10	8.70	9.70	10.90	10.00
Layer thickness (km)	2.8 ± 1.4	1.40 ± 0.91	1.45 ± 0.87	1.36 ± 0.86	1.47 ± 0.86	1.37 ± 0.88	1.39 ± 0.97	1.35 ± 0.89
		1.22	1.31	1.15	1.35	1.21	1.19	1.17
		0.81	1.16	0.45	0.99	0.63	0.45	0.63
Temperature (K)	231 ± 11	227.97 ± 10.03	228.8 ± 9.43	226.84 ± 10.67	228.60 ± 9.56	228.35 ± 9.51	225.79 ± 10.60	230.50 ± 9.57
		227.53	228.40	226.23	228.27	228.28	224.85	229.39
		224.00	228.00	224.00	228.00	232.00	224.00	224.00
Layer top–tropopause distance								
dBZ_e		−29.61 ± 9.07	−29.39 ± 8.76	−29.98 ± 9.49	−29.26 ± 8.58	−29.41 ± 8.90	−30.62 ± 9.56	−28.55 ± 8.85
		−29.69	−29.16	−30.47	−29.02	−28.95	−31.30	−28.76
		−33.70	−21.70	−33.70	−32.80	−24.30	−34.70	−29.20
ECMWF vertical motion (cm s^{-1})		0.06 ± 1.80	0.10 ± 1.82	0.05 ± 1.70	0.04 ± 1.83	0.00 ± 2.14	0.00 ± 1.44	0.11 ± 1.78
		−0.08	0.00	−0.13	−0.09	−0.08	−0.17	0.10
		−0.30	−0.30	−0.30	−1.30	−1.10	−0.30	−0.10
NCEP vertical motion (cm s^{-1})		0.10 ± 1.74	0.17 ± 1.96	0.08 ± 1.49	0.19 ± 1.96	−0.01 ± 1.93	0.10 ± 1.38	0.16 ± 1.70
		0.06	0.22	−0.01	0.28	−0.07	−0.01	0.14
		−0.10	0.60	−0.10	0.80	−0.20	−0.20	0.10
Z_e		−21.59 ± −17.02	−22.39 ± −18.88	−20.84 ± −15.93	−22.59 ± 19.48	−22.28 ± −18.95	−21.03 ± −16.02	−20.62 ± −15.82
		−29.69	−29.16	−30.47	−29.02	−28.95	−31.30	−28.76
		−43.98	−43.98	−43.01	−43.98	−46.99	−43.01	−41.55
IWP (g m^{-2})		18.0 ± −24	18.6 ± −23	17.7 ± −26	18.5 ± −21.7	18.3 ± −23.5	17.2 ± −26.0	18.5 ± −23.4
		8.0	9.2	6.9	9.7	8.2	6.7	8.3
IWC (g m^{-3})		0.012 ± −0.013	0.012 ± −0.012	0.011 ± −0.013	0.012 ± 0.012	0.011 ± −0.013	0.012 ± −0.014	0.012 ± −0.014
		0.007	0.007	0.007	0.007	0.006	0.008	0.008
r_e (μm)		36.4 ± −17.4	35.5 ± −15.3	36.6 ± −19.4	35.6 ± −14.9	35.6 ± −15.8	35.8 ± −19.2	39.2 ± −19.0
		33.9	33.6	33.2	33.5	34.7	31.7	36.7
τ		0.77 ± −0.95	0.79 ± −0.91	0.76 ± −1.01	0.79 ± −0.89	0.78 ± −0.95	0.74 ± −1.01	0.79 ± −0.95
		0.39	0.43	0.36	0.45	0.39	0.35	0.39
ε		0.32 ± 0.25	0.33 ± 0.25	0.31 ± 0.36	0.33 ± 0.24	0.32 ± 0.26	0.30 ± 0.26	0.32 ± 0.26
		0.25	0.26	0.24	0.27	0.25	0.23	0.25

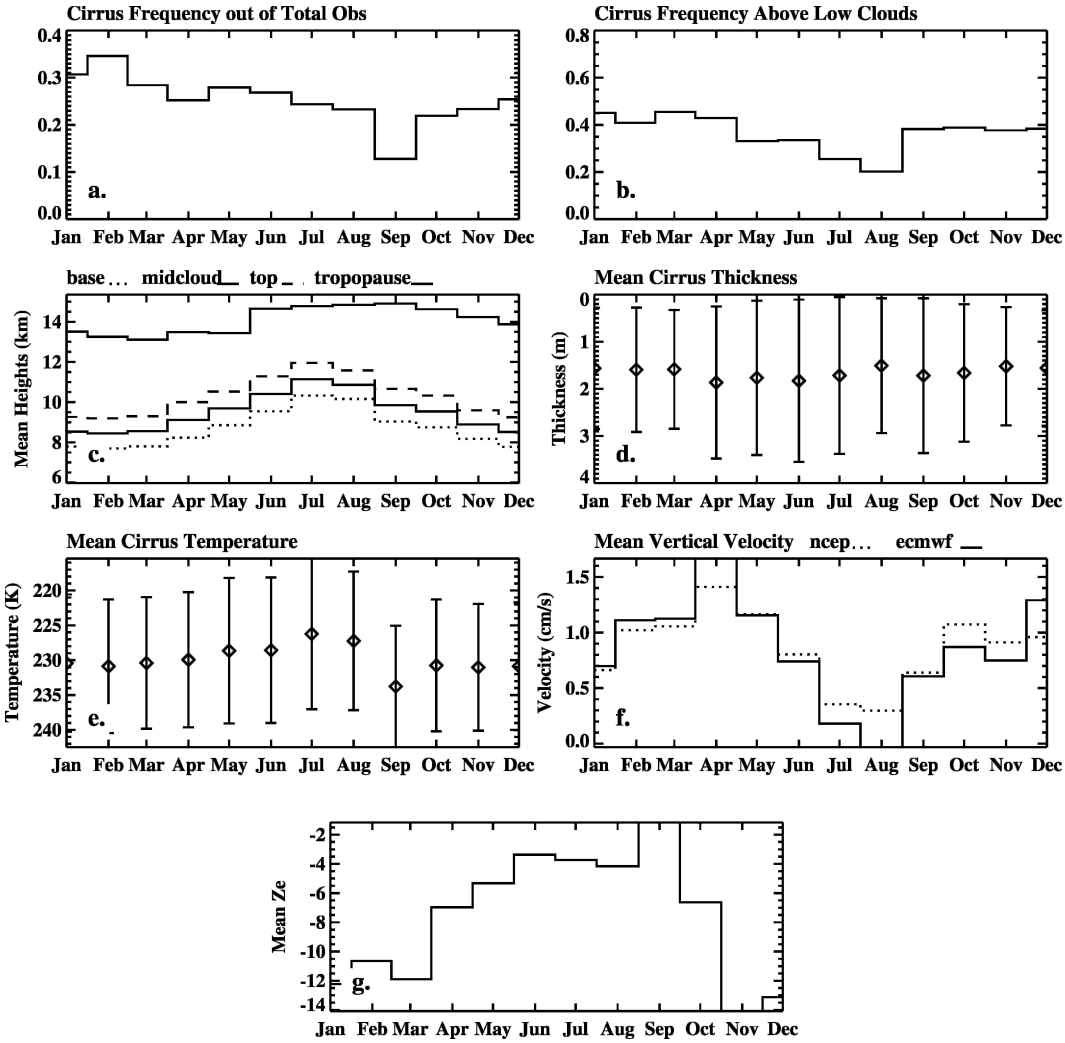

FIG. 3. As in Fig. 2, but shown as a composite annual cycle.

rally limited to optical depths near 3 by the attenuation of the lidar system.

We do find a weak diurnal cycle in cirrus occurrence (Fig. 4) at the ACRF. In both the warm and cold seasons (May–September and November–March, respectively) we find that cirrus tend to be most likely in the early evening hours, presumably due to the increased likelihood of convective outflows during the evening. During the cold season, the minimum in occurrence seems to occur in the early local morning while the summer minimum is in the late local afternoon near the end of the UTC day. In both seasons the range between the diurnal maxima and minima is approximately 7% or about 1/4 of the mean occurrence. We also find that the layering of cirrus above lower-level clouds has a reasonably well-defined diurnal cycle with cirrus most likely to be found above lower-level clouds during the local daytime (presumably due to the occurrence of boundary layer clouds) with the warm season showing a cycle of more amplitude although the mean value of layering during the cold season is larger overall by about 10%.

4. The large-scale atmosphere and cirrus occurrence

In M97 and M01 we examined the large-scale vertical motion associated with cirrus cloud occurrence. In both studies, we found that the mean value of large-scale vertical motion was weakly positive ($+0.7$ cm s^{-1} in M97 and $+0.2$ cm s^{-1} in M01) but that the large-scale vertical motion is nearly as likely to be descending as ascending when cirrus are observed, making this quantity unlikely to be effective as the sole input to cloud

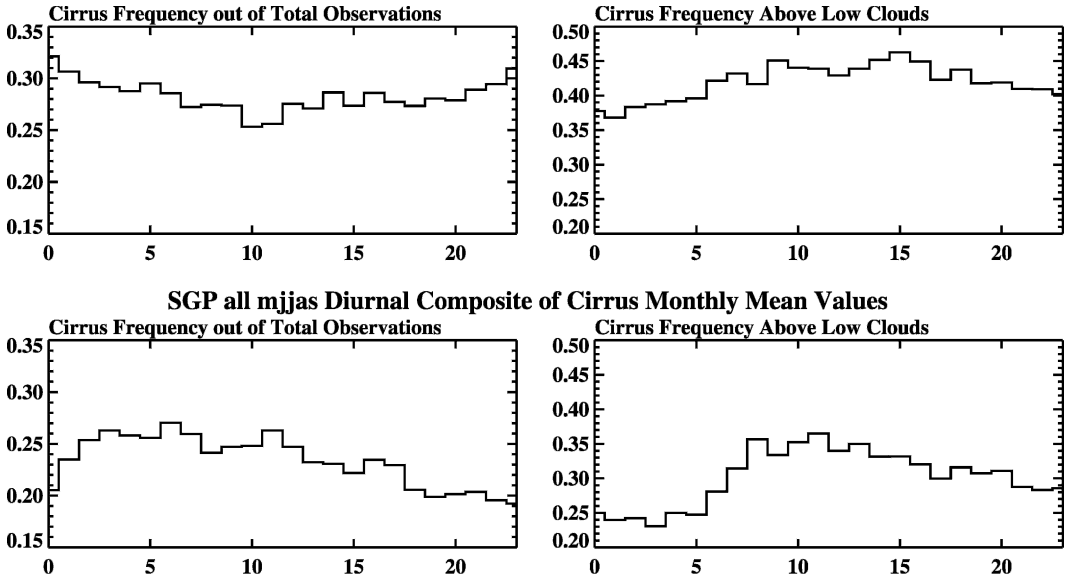

FIG. 4. Composite diurnal cycle of cirrus occurrence for the warm season (MJJAS) and the cold season (NDJFM). The abscissa in these plots are time in UTC. Local noon is approximately 1700 UTC, and 0000 UTC corresponds to early local evening.

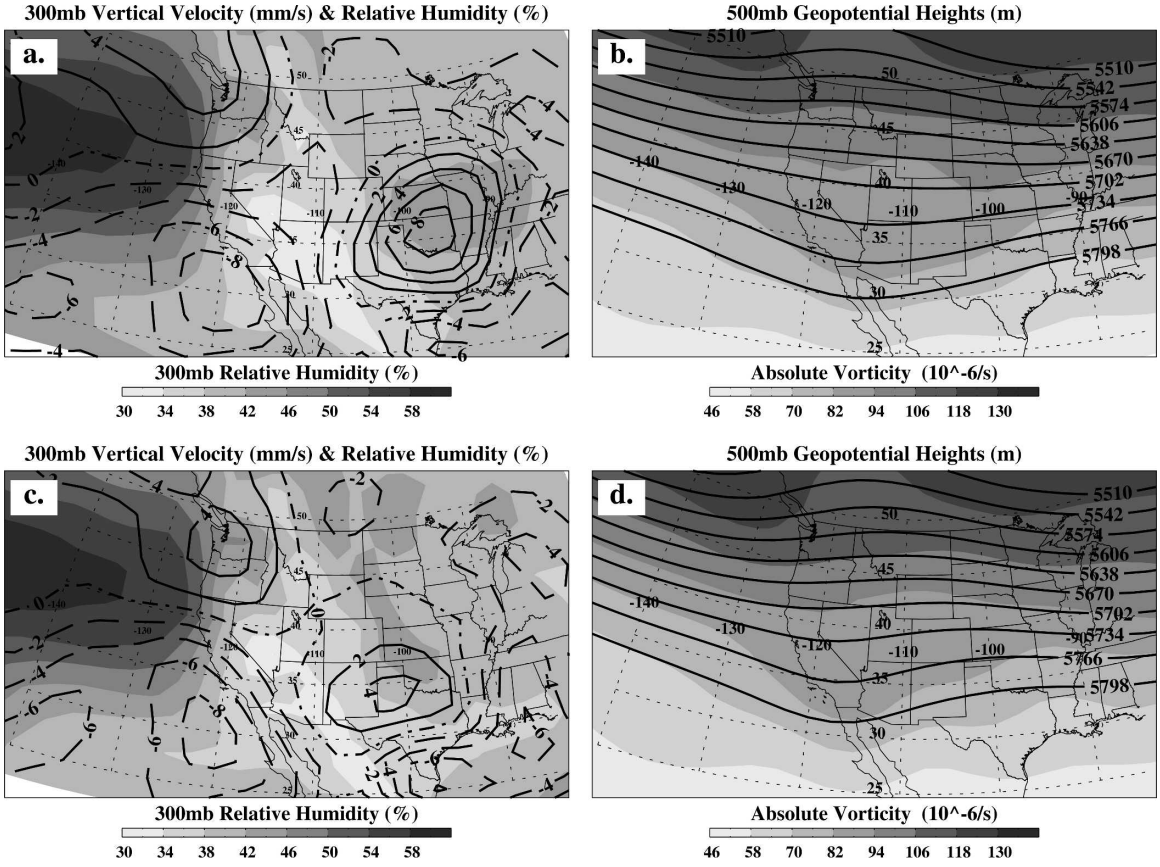

FIG. 5. NCEP–NCAR mean meteorological patterns when cirrus are observed at the ACRF by the MMCR. (a), (c) The 300-hPa vertical motion (contours) and relative humidity with respect to water; (b), (d) the 500-hPa heights and absolute vorticity. Panels (a) and (b) are for the full cirrus dataset, while (c) and (d) are for the thin cirrus subset to which the *Z–R* retrieval algorithm have been applied. The ARM Climate Research Facility is located in north-central Oklahoma.

parameterizations such as proposed by Heymsfield and Donner (1990). We did show, however, in M01 that, as the large-scale ascent in the upper troposphere increased, cirrus were increasingly likely to be encountered. While ascent on some spatial scale is certainly required to nucleate and maintain cirrus layers, given the time scales associated with ice crystal growth and sublimation (Khvorostyanov and Sassen 1998) this ascent may not necessarily need to occur nearby or be resolved on large scales. Here we revisit this question and consider other aspects of the large-scale atmosphere when cirrus are observed by the MMCR over the ACRF.

In Fig. 5 we show the mean vertical motion and relative humidity (RH) at 300- and 500-hPa heights and absolute vorticity as diagnosed by the NCEP–NCAR reanalysis when cirrus were observed by the MMCR at the ACRF. For both AllCi and ThCi, the ACRF is within a southwesterly flow at 500 hPa with a split flow over western North America. For AllCi the geopotential heights at 500 hPa are approximately 20 m lower and the trough axis is not so far upstream as compared to ThCi. In both cases, upper-tropospheric ascent is diagnosed in the region around the ACRF during cirrus events with the area of ascent for AllCi centered over Oklahoma with an average magnitude of approximately 0.8 cm s^{-1}. The ascending region extends westward into New Mexico and eastward into the Mississippi Valley. In ThCi, ascent is also diagnosed on average although it is substantially weaker (0.4 cm s^{-1}) with a center situated over the Texas Panhandle. For ThCi, the ARM site is actually situated in a region where the ascent is weakening on average as the air moves through the southwesterly flow.

The long-term averages do, however, mask a large degree of variability in the large-scale dynamics. Figure 6 shows the vertical motion histograms for the various classes of cirrus. We also compare the NCEP results to output from the ECMWF model. While there are quantitative differences between the models, the qualitative interpretations are similar. Consistent with the findings of M97 and M01, it seems clear that, while the overall large-scale ascent tends to be positive, cirrus are nearly as likely to be found in descending air masses as ascending. Stubenrauch et al. (2004) found the majority of the cirrus that they examined existed in environments where the large-scale vertical motion was less than about ± 1.5 cm s^{-1}. The small net positive vertical motion, found here, arises in part because the frequency distributions are slightly skewed toward positive values. This skewness is particularly evident when comparing the single layer thin cirrus to the thick layers

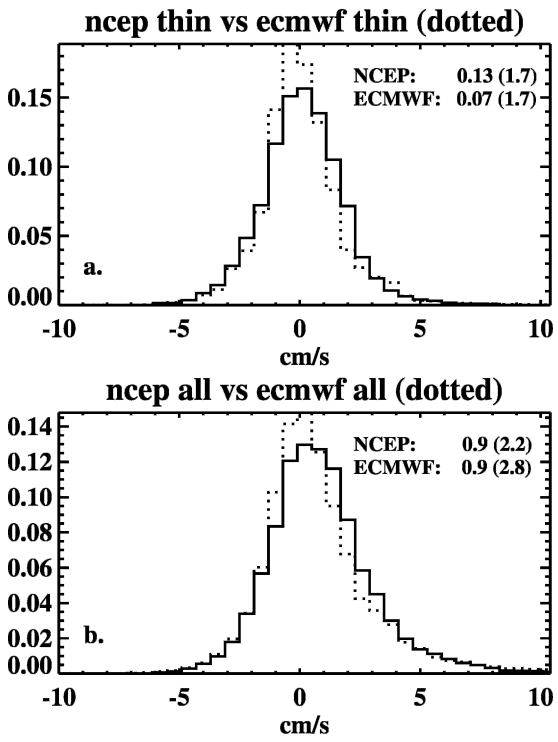

FIG. 6. Frequency distributions of large-scale vertical motion at 300 hPa from the NCEP–NCAR reanalysis and the ECMWF model over the ACRF when cirrus are observed by the MMCR: (a) the thin cirrus subset and (b) the full cirrus dataset. In both plots the ECMWF vertical motion histogram is dotted.

where the primary differences are decreased frequency of larger-scale ascent greater than 2 cm s^{-1} and an increased frequency of occurrence near 0 cm s^{-1} for the thin cirrus population.

While it is reasonably well established that mesoscale turbulence, which could continue to generate cirrus, can exist within an atmosphere that is weakly descending on the synoptic scale, the modeling results of Starr and Cox (1985) suggest that cirrus cannot be maintained in subsident conditions for extended periods. However, cirrus entering subsidence regions from regions of large-scale ascent do decay over some finite period. Given Starr and Cox's model results and the weak subsidence in the vicinity of the ridge axis, this decay would occur over a period of 1–2 h along trajectories that may extend several hundreds of kilometers downstream of the ascending region. Furthermore, ice crystals, unlike liquid water droplets, do have a time scale that is fairly long. Heymsfield and Donner (1990) suggested that cirrus particles can fall through subsaturated air for several kilometers before fully sublimating. A combination of these phenomena likely contribute to our finding that, while thicker and more persis-

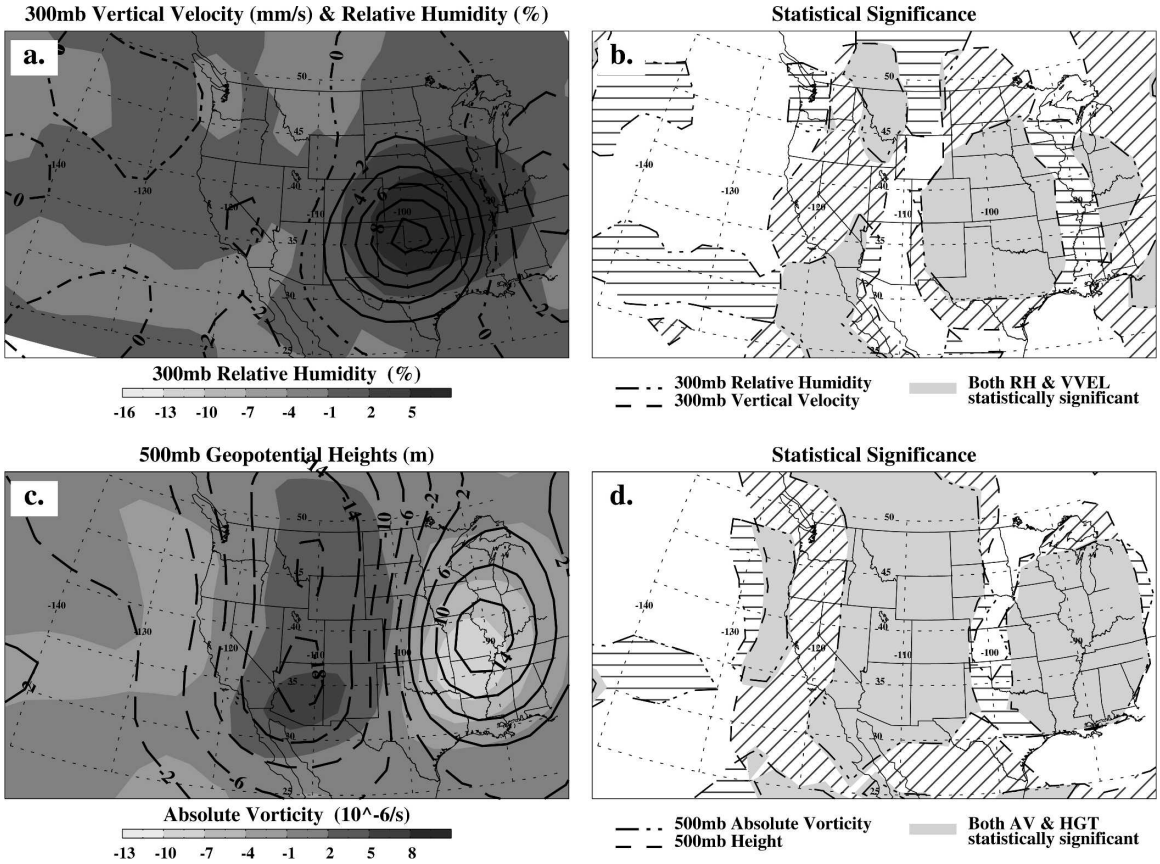

FIG. 7. NCEP cold-season all-cirrus anomalies from (a) 300-hPa vertical motion and RH anomalies and (b) statistical significance of the 300-hPa anomalies; (c) 500-hPa heights and vorticity anomalies calculated from the NCEP–NCAR reanalysis and (d) statistical significance of the 500-hPa anomalies. This figure shows results for all cirrus events during the cold season as opposed to Fig. 8, which shows cold season results for thin cirrus.

tent cirrus are found in large-scale ascent, thinner cirrus are not uncommon in regions of weak subsidence.

To examine the large-scale meteorology in more detail and minimizing any model biases that might exist, the anomalies of various meteorological quantities from the 30-yr mean, extracted from the NCEP–NCAR reanalysis, are shown in Figs. 7–10 where we divide the dataset by season. As in M01, we define the warm season as the period from May through September (MJJAS) and the cold season as the period from November through March (NDJFM). We find that the anomaly patterns and their statistical significance on the synoptic scale are similar across the seasons and cirrus classes with subtle yet important differences. In general, the anomalies are significantly different from climatology in the region extending from the Mississippi Valley through the desert southwest of the United States. The cold season anomalies, when cirrus are forced primarily on the large scale, are significant over a broader geographic region that extends into the Pacific Northwest. In general, we find that the vorticity statistical significance is less well established than the geopotential heights.

Considering the pattern at 500 hPa, cold season cirrus are found to occur upstream of the large-scale ridge axis and downstream of the inflection point between negative and positive geopotential height anomalies, while thin cirrus during the cold season are found to occur, on average, very near the 500-hPa ridge axis. During the cold season, vertical motion anomalies in the upper troposphere are positive for AllCi with the maximum of 1.1 cm s^{-1} displaced upstream of the ACRF location in southwestern Oklahoma near the Texas Panhandle although the maximum in upper-tropospheric humidity tends to be centered near the observing site. For ThCi during the cold season, the peak in upper-tropospheric vertical motion is centered farther upstream and is elongated to the southwest of the ACRF with a weaker maximum value of 0.9 cm s^{-1}.

During the warm season, the synoptic-scale systems

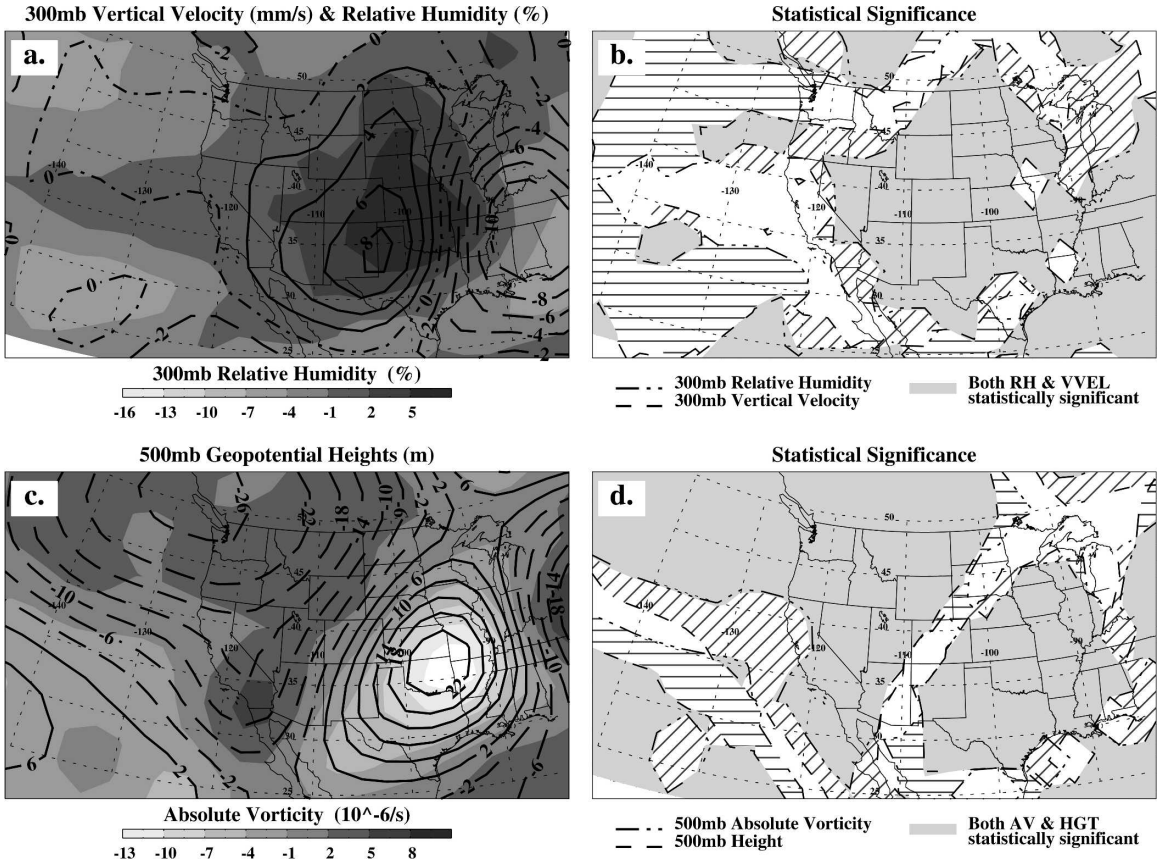

FIG. 8. As in Fig. 7, except for the thin cirrus subset.

are weaker or totally absent and a substantial fraction of the clouds in the upper troposphere are associated with moisture that has been detrained from deep convective systems. There is a general decreasing occurrence of cirrus during this time of year with May and June being the peak months when synoptic-scale dynamics and solar heating combine to generating deep convection that produces periods of persistent upper-tropospheric clouds. The 500-hPa height anomalies are found to be generally smaller and less significant than during the cold season when cirrus are observed at the ACRF, although a region of low heights and positive vorticity in the southwestern United States and a weak ridge axis situated near or over the ACRF seems to be common. The vertical motion patterns in the upper troposphere do show positive anomalies during warm season cirrus events that are reasonably similar to those found in the cold season. The vertical motion anomalies are somewhat weaker and tend to be situated directly over the ACRF. While upper-tropospheric ascent is expected during the cold season to be an important maintenance mechanism for cirrus cloud systems, positive vertical motion during the warm season would not seem to be necessary if most of the cirrus clouds were simply caused by detrainment from deep convection. It would appear from these results, however, that large-scale ascent continues to be a reasonably important component of cirrus cloud maintenance during the warm season.

5. The bulk microphysical and radiative properties

To the ThCi subset, we apply the ZR algorithm (Mace et al. 1998, 2005) to estimate the effective particle size (r_e), the condensed water path (IWP), the 11-μm IR beam emittance (ε), and the visible optical depth (τ), where τ is derived using the parameterization described by Fu and Liou (1993) that takes the IWP and r_e as input. We also calculate layer-mean ice water content (IWC) by normalizing the IWP with the layer thickness. The frequency distributions of these quantities are shown in Fig. 11 and the results summarized in Tables 3 and 4. The overall 6-yr statistics are very similar to those reported in M01. Similar distributions of optical depth have recently been reported by Comstock et al. (2002) derived from tropical cirrus data, and the mean values reported here compare well to those re-

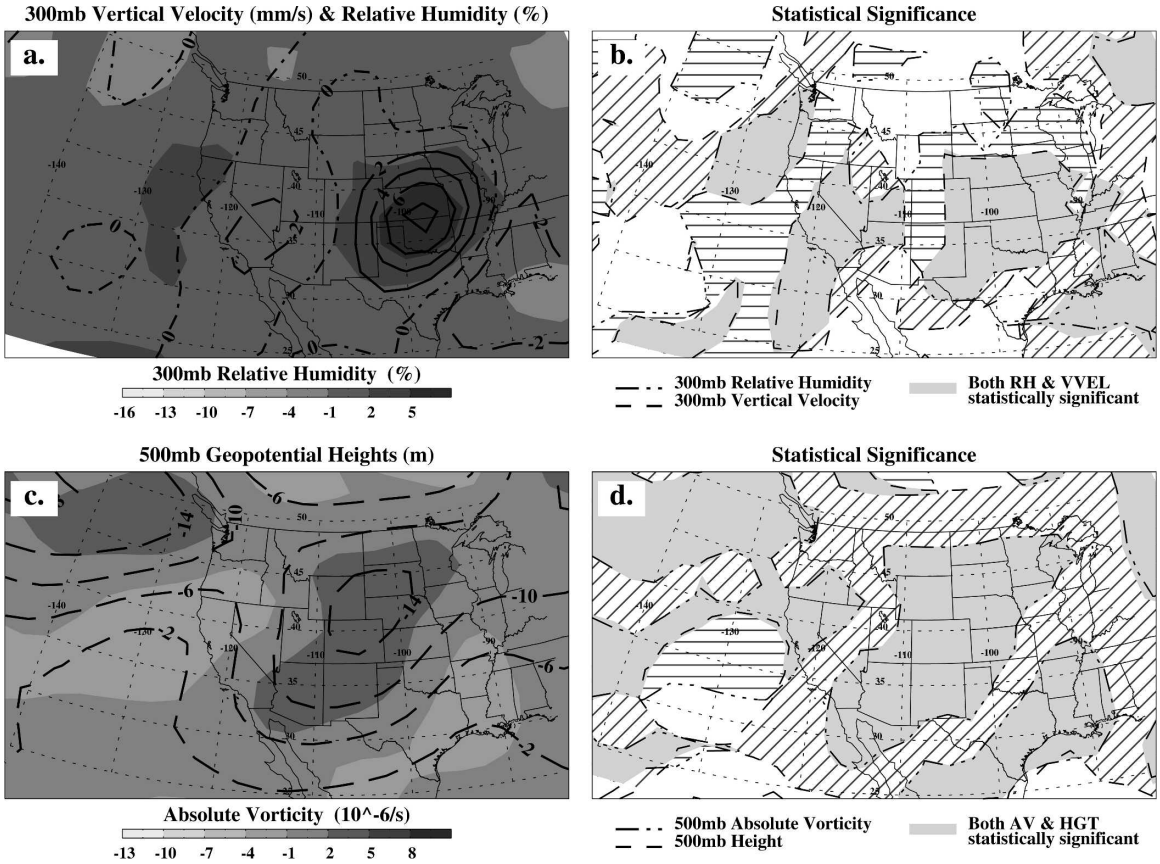

FIG. 9. NCEP warm season all-cirrus anomalies from (a) 300-hPa vertical motion and RH anomalies, and (b) statistical significance of the 300-hPa anomalies; (c) 500-hPa heights and vorticity anomalies calculated from the NCEP–NCAR reanalysis and (d) statistical significance of the 500-hPa anomalies. This figure shows results for all cirrus events during the warm season as opposed to Fig. 10, which shows warm season results for thin cirrus.

ported by Sassen and Comstock (2001) who applied a modified lidar–radiometer (LIRAD) technique (Platt and Dilley 1981) to derive the radiative properties of cirrus observed over northern Utah. For τ, Sassen and Comstock report 0.75 ± 0.91 and for ε they report 0.30 ± 0.22. The respective quantities from our dataset are 0.78 ± 0.95 and 0.32 ± 0.25.

Unlike Stubenrauch et al. (2004), we find little variation in the statistics of the bulk microphysical and radiative properties between the warm and cold seasons even though the warm season cirrus exist in a deeper troposphere that extends to colder temperatures, and they exist in a very different dynamical regime than the cold season clouds. To some extent, the large water path extremes of these distributions are determined by the restrictions of our analysis technique where we require optically thin single-layer clouds. However, that we find variations as a function of large-scale ascent (discussed below) suggests that, were there to be any substantial variations in the ThCi subset, there should be some evidence of it in the probability distribution functions. We find, also, that the IWC distributions are approximately exponential with similar means and standard deviations. The IWP frequency distribution departs somewhat from an exponential shape with the standard deviation somewhat larger than the mean. This difference is caused by the large IWP tails of the distributions where rarely occurring geometrically thick but optically thin layers are included. This departure from an exponential-type distribution may be an artifact of the sampling since geometrically thick layers of high IWP have the potential to be optically thick depending on particle size and, therefore, the PDFs are not necessarily representative of an unrestricted distribution of cirrus layers. Here r_e is distributed more normally than the IWP and IWC although the distribution is skewed slightly toward larger values. While we find no significant seasonal dependencies in the statistics of r_e, the occurrence of large particles seems to be more common during the warm season.

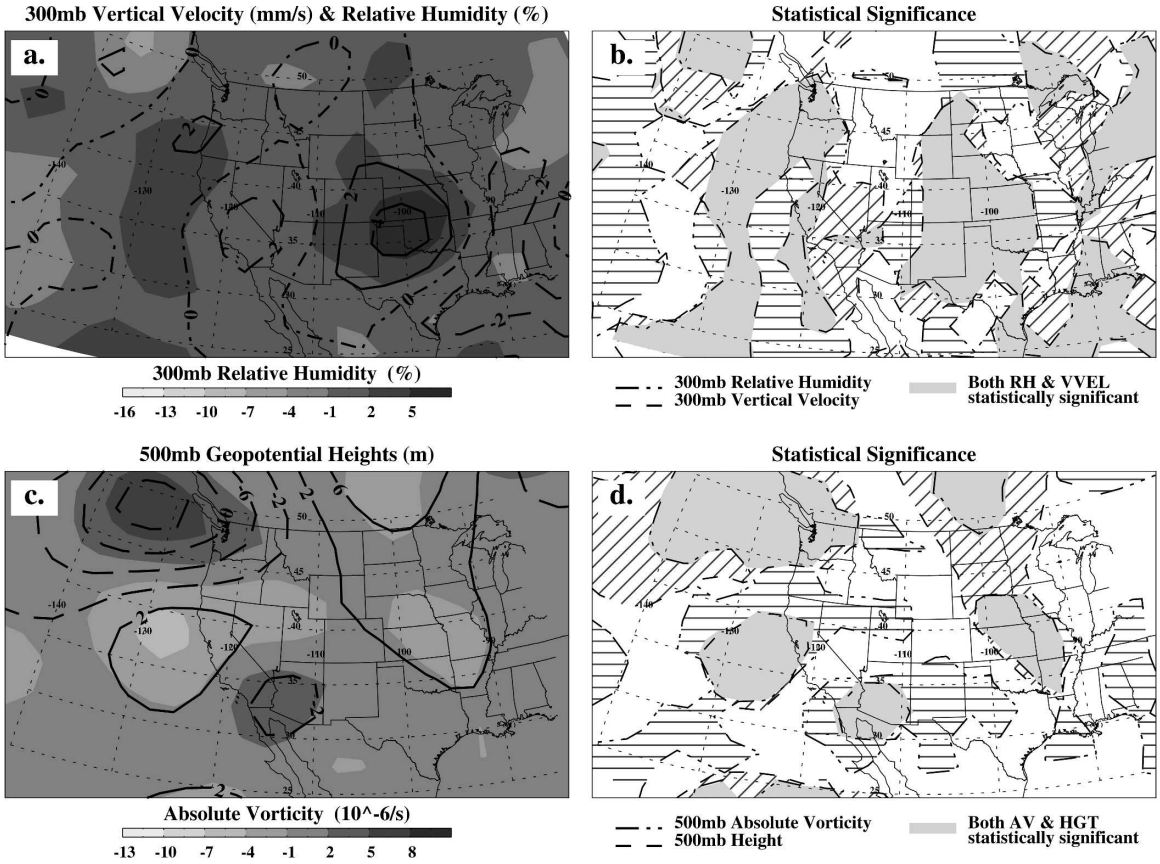

FIG. 10. As in Fig. 9, except for the thin cirrus subset.

With 6 years of data we are able to examine the record for additional variability and long-term trends that are not represented in the seasonal PDFs of the cloud properties. In Fig. 12 we show time series plots of the seasonal means and event standard deviations of IWP, and effective radius. Two different measures of variance are shown in Fig. 12. Within each cirrus event we calculate the standard deviation of the IWP and effective radius and plot the mean of this intraevent standard deviation ($\overline{\sigma}^{x}_{\text{in}}$; x represents either the IWP or r_e) as the thin vertical bar on the time series. Also of interest is the interevent standard deviation (σ^{x}_{Ev}) that measures how widely varying the events are during a season; σ^{x}_{Ev} is plotted as the thick vertical line in Fig. 12. There appear to be only slight deviations in the seasonal means during the 6-yr period with no evidence for long-term trends. The absence of long-term trends in the retrieved cloud properties suggests stability in the MMCR and AERI observations. We do, however, find interesting seasonal dependencies in the variability of the bulk microphysical properties of cirrus events. While there are exceptions, on average the variability in the cold seasons tends to be smaller than the variability in the warm seasons. This is particularly evident in $\sigma^{\text{IWP}}_{\text{Ev}}$ where the cirrus events during the cold seasons are much less variable than cirrus events during the warm seasons; $\overline{\sigma}^{\text{IWP}}_{\text{in}}$ does not demonstrate a clear seasonal variation. This suggests that the IWP varies less within events than events themselves vary from one another. There also does not appear to be a clear seasonal dependence in $\sigma^{r_e}_{\text{Ev}}$ or $\overline{\sigma}^{r_e}_{\text{in}}$, although the cold seasons, on average, tend to have lesser values of $\sigma^{r_e}_{\text{Ev}}$ and $\overline{\sigma}^{r_e}_{\text{in}}$ than do the warm seasons.

6. Sensitivity of the microphysical properties to large-scale vertical motion

Because cirrus are often embedded in fast-moving air currents, particularly in the middle-latitude cold season, cirrus are often viewed conceptually as entities advecting passively as "blowoff" from the nearest deep cloud system. Numerical models of cirrus as well as observational studies have suggested, however, that that vertical motion on large scales is important to the maintenance of these cloud systems against particle sedimentation (Starr 1987; Lin et al. 2005). In M01 with a

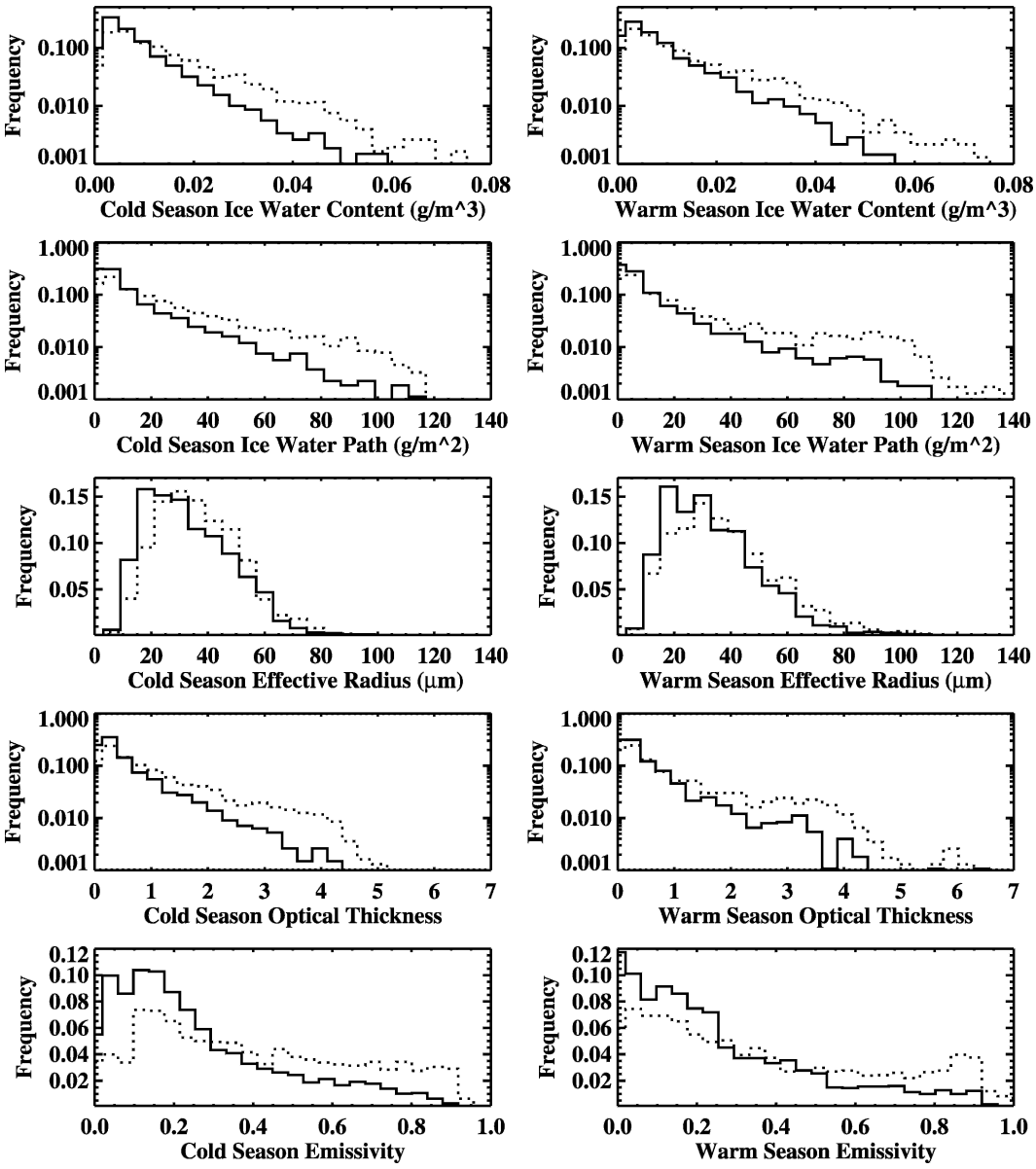

FIG. 11. Frequency distributions of cirrus properties in the (left) cold and (right) warm seasons for downward (solid) and upward (dotted) large-scale synoptic conditions as derived from coincident NCEP reanalysis data.

dataset that spanned just 1 year, we did find a weak dependence in the particle size to the magnitude of the large-scale ascent, although the statistical significance of that inference was suspect. In the previous section, however, we show that the thin cirrus dataset to which we applied the ZR algorithm tended to occur in weaker larger-scale ascent than the full dataset. In Fig. 11 and Table 4 we compare the seasonal bulk microphysical distributions in situations where the large-scale ascent is positive and negative. While r_e shows only a slight variation, the IWC and IWP distributions are quite different as a function of large-scale vertical motion. During the cold season, the mean IWC and IWP both increase by nearly a factor of 2 when cirrus are observed in air ascending on large scales as compared to cirrus observed in large-scale subsidence. Similar increases are found during the warm season although the changes in the distributions are not quite so striking.

During the cold season, we find approximately similar changes to the IWC and the IWP distributions. The frequency of occurrence of IWC (IWP) values below 0.01 g m^{-3} (10 g m^{-2}) decreases, while the frequency of occurrence of values greater than 0.01 g m^{-3} (10 g m^{-2}) increases by nearly equal fractional amounts out to val-

TABLE 4. Statistics of microphysical and radiative properties of thin cirrus derived using the *Z–R* algorithm. Shown are the indicated quantities (mean, standard deviation, and median) during the cold and warm seasons in large-scale ascent (up) and large-scale subsidence (down).

			Mean	Std dev	Median
IWC (g m^{-3})	Cold	Up	0.015	0.014	0.010
		Down	0.009	0.010	0.006
	Warm	Up	0.014	0.015	0.009
		Down	0.009	0.010	0.006
IWP (g m^{-2})	Cold	Up	24.3	25.8	14.6
		Down	12.7	17.5	5.7
	Warm	Up	24.0	20.5	10.2
		Down	12.8	20.4	4.9
r_e (μm)	Cold	Up	37.2	15.7	35.7
		Down	33.7	15.7	31.1
	Warm	Up	38.7	19.5	36.0
		Down	34.5	18.2	30.9
τ	Cold	Up	1.03	1.06	0.65
		Down	0.56	0.69	0.29
	Warm	Up	1.01	1.19	0.49
		Down	0.57	0.82	0.26
ε	Cold	Up	0.40	0.26	0.35
		Down	0.26	0.21	0.19
	Warm	Up	0.37	0.29	0.30
		Down	0.25	0.23	0.19

ues of 50 g m^{-3} (100 g m^{-2}). This suggests that the changes in the cloud layers are not totally due to increasing geometrical thicknesses of the layers but due to actual changes in the water contents of the layers themselves. During the warm season, the changes in the IWP distribution appear to occur preferentially at the larger water paths, although the changes to the distribution of IWC during the warm season are similar to the cold season, suggesting that the increases in the mean values of IWC and IWP come about due to both an increase in geometrical thickness and higher overall water contents in the ascending air masses.

To further explore the relationship between the water contents and large-scale vertical motion, we take the IWP PDF combined for the cold and warm seasons for all vertical motions and identify the third of these cirrus events with the lowest IWP and the third of events with the highest IWP. For both of these subsets, we compute the 300- and 500-hPa anomalies as in Fig. 7 and plot them in Figs. 13 and 14. We find that the third of events with the lowest values of IWP tend to be found just downstream of the 500-hPa ridge axis in an area of weakly descending air. Interestingly, we find positive vertical motion anomalies upstream of the ACRF when the thinnest cirrus are observed there, suggesting that the cirrus with the lowest IWP had passed through an area of ascending air before they were observed by the MMCR and, at the time of observation, were in the process of dissipating in the large-scale subsidence. Starr and Wylie (1990) and Sassen et al. (1989) discuss case studies that exemplify this process. In contrast, the third of cirrus with the highest IWP were found upstream of the 500-hPa ridge axis and resided in ascending air where the center of ascent was very near or just upstream of the ACRF [see also Starr and Wylie (1990) for a case study]. These thicker clouds were found in a pronounced humidity maximum in the upper troposphere while the thinner cirrus were associated with a much weaker humidity maximum that was centered over the Oklahoma and Texas Panhandle region.

7. Summary and conclusions

Using ground-based remote sensing data collected at the ACRF during a 6-yr period, we have examined the statistics of cirrus cloud occurrence and bulk microphysical properties. So that we could consider the relationships between the clouds and their large-scale environment, we combined the ground-based data with coincident NCEP–NCAR reanalysis data and diagnostic information from the ECMWF model. We define cirrus based on the cloud-top temperature, the temperature of the layer-maximum radar reflectivity factor, and the temperature of cloud base using a reasonably flexible approach as defined in Eq. (1) and Table 2. This technique allows us to avoid thick mixed phase layers or ice phase layers that top deeper cloud systems and to consider only layers that would normally be classified as cirrus by a ground observer. Over the 6-yr period, approximately 11 000 h of cirrus data were collected by the MMCR. Approximately 2500 h of that total were single-layer thin cirrus to which we were able to apply the *Z–R* cloud property retrieval algorithm (Mace et al. 1998, 2005).

We find that cirrus are observed over the ACRF between 25% and 30% of the time (Figs. 2 and 3) with occurrence peaks in January and May of typical years. The frequency of occurrence of cirrus by month ranged between 10% and 40% during the 6 years considered. Minima in frequency tended to occur in late summer when overall cloud activity over the region is low and maxima in occurrence were found in late winter and spring when synoptic-scale storm systems and strong jet streams are associated with deep convection. Of the total, cirrus were observed to occur above lower-level clouds roughly 1/3 of the time—more during winter

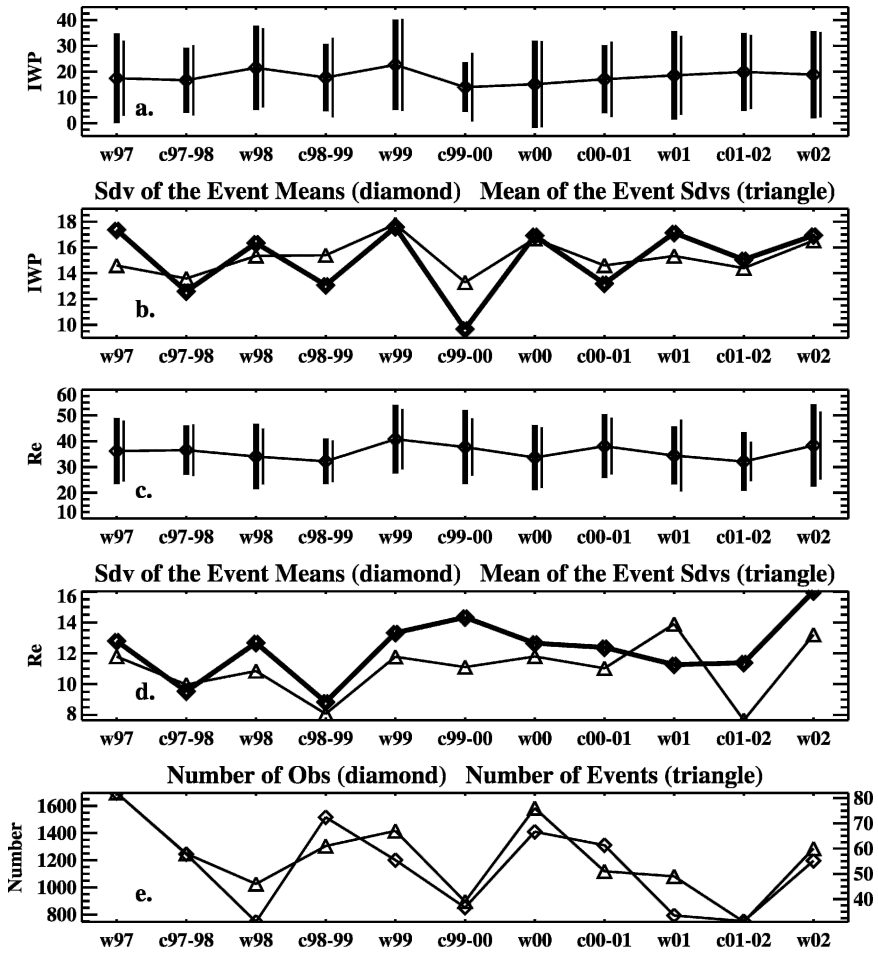

FIG. 12. Seasonal time series of IWP and effective radius for the thin cirrus subset derived with the *Z–R* algorithm: (a) The mean and standard deviation of IWP. The thin and thick vertical lines refer to the intra- and interevent standard deviations, respectively (see text for additional details). (b) Plots of the intra- (thin lines) and interevent standard deviations of IWP. (c), (d) As in (a) and (b), except for effective radius. (e) The number of (right-hand ordinate) events and (left-hand ordinate) observations as a function of season.

than summer. We find little variance in the mean temperature of cirrus layers, and the base and top heights of the layers increased and decreased with the seasonal deepening and thinning of the troposphere over this region. Our temperature-based definition likely contributes to this finding, although our statistics agree well with those reported by Sassen and Campbell (2001) who considered a decade-long climatology of cirrus observations collected with lidar over northern Utah.

The large-scale meteorological patterns over the Southern Plains region when cirrus were observed at the ACRF was examined using anomaly plots of geopotential heights and vorticity on the 500-hPa surface and vertical motion and relative humidity on the 300-hPa surface (Figs. 7–10). During the cold season, cirrus were found in ascending moist air in the upper troposphere upstream of a 500-hPa ridge. Typically a trough axis was found over Arizona. This pattern was less pronounced during the warm season although ascent in the upper troposphere was common to both seasons when cirrus are observed at the ACRF. The upper troposphere in regions of cirrus was found to be ascending on average with the region of ascent typically situated just upstream of the observing site. The NCEP–NCAR reanalysis data tended to diagnose enhanced relative humidity in the region, consistent with the large-scale vertical motion patterns.

While we find little seasonal variation in the bulk microphysical properties, we do find a correlation between the bulk microphysics and the large-scale vertical motion. On average, the large-scale ascent at 300 hPa

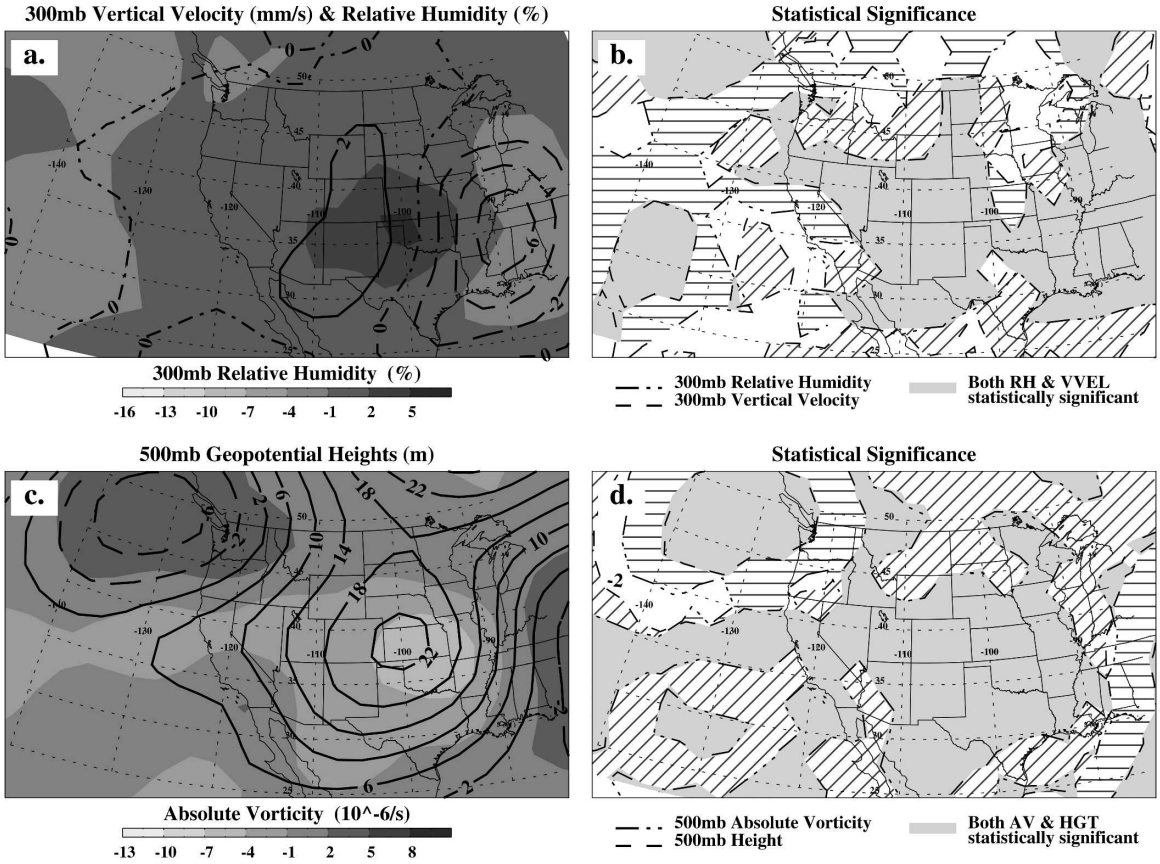

FIG. 13. As in Fig. 7, except for the cirrus that populate the lower third of the thin cirrus IWP frequency distribution.

diagnosed by the NCEP–NCAR reanalysis data was 0.88 ± 2.2 cm s^{-1} while the ECMWF model diagnosed 0.88 ± 2.8 cm s^{-1}. For the optically thin single-layer subset, the large-scale vertical motion was 0.13 ± 1.7 cm s^{-1} and 0.07 ± 1.7 cm s^{-1} for the NCEP–NCAR and ECMWF models, respectively. Cirrus observed during the cold season tended to exist in slightly stronger vertical motion. The optically thin subset of cases, for instance, had a mean ascent of 0.25 cm s^{-1} during the cold season months and 0.07 cm s^{-1} during the warm season. As can be seen by the standard deviations about the means, the spread of the distributions is large (Fig. 6), and a substantial fraction of the observed cirrus occurred in large-scale subsidence. We examined the bulk microphysical properties of the clouds in the ascending and subsident regions and, indeed, found that the amount of condensed water mass was larger by nearly a factor of 2 during the cold season in the ascending events. The particle sizes showed no significant change as a function of large-scale vertical motion.

Overall, these results paint a fairly clear picture of the association between cirrus clouds, as we define them, and the large-scale meteorology in the vicinity of the observing site. During the cold season months, cirrus form in the ascending region of the upper troposphere downstream of evolving middle-latitude disturbances. These disturbances tend to be manifested as troughs in the middle-tropospheric geopotential height field with accompanying low pressure systems over arid regions of Texas and New Mexico. Cirrus are found to exist typically just downstream of a maximum in upper-tropospheric ascent and have likely undergone a period of ascent as the air moved through flow. The cirrus regions are also typically embedded in a maximum of upper-tropospheric water vapor anomaly as diagnosed by the NCEP–NCAR reanalysis. The optically thinnest cirrus tend to occur, on average, in large-scale subsidence just downstream of the upper-level ridge axis, and the clouds tend to thicken upstream of the ridge axis where the large-scale ascent is positive. Starr and Wylie (1990) referred to this phenomenon as "ridge-crest" cirrus. On average, the thickest cirrus layers are found nearer the circulation anomaly inflection points where large-scale ascent is increasing. Upstream of the

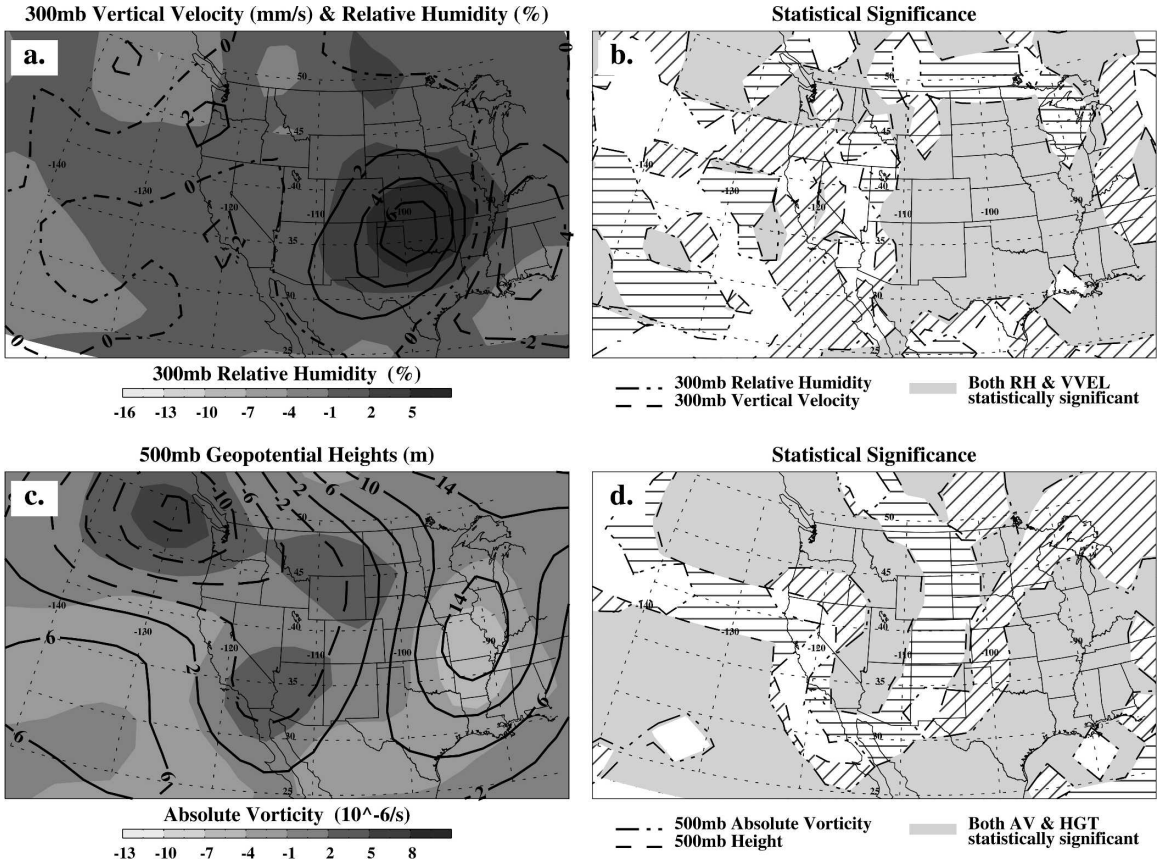

FIG. 14. As in Fig. 7, except for the cirrus that populate the upper third of the thin cirrus IWP frequency distribution.

inflection points, the clouds are typically deep and are not classified as cirrus using our definition.

In the summer, the picture is somewhat different. While ascent in the upper troposphere still seems to be frequently observed, the ascent anomalies are much less distinct and tend not to be displaced upstream of the observing location. This result is consistent with the assumption that warm season cirrus tend to be formed more in association with moisture detrained from deep convection although, given the existence of both a vertical motion and humidity anomaly at 300 hPa, the cirrus do not appear to be simply sublimating anvils resulting from convective detrainment, but may be actively maintained for some period of time by upper-tropospheric dynamics.

This study raises a number of questions that will form the nucleus of our future research in this area. The ARM program operates several sites in the tropical western Pacific where cirrus are ubiquitous. We have found that tropical cirrus persist many hours beyond what would be expected from simple sedimentation of detrained ice crystals (Mace et al. 2006). The mechanism for this longevity is presently unknown, but understanding such questions is important to the successful parameterization of these clouds in climate models.

From a climate feedback standpoint, the relationships found here between cirrus occurrence, their bulk properties, and the large-scale dynamics suggest that the radiative feedbacks associated with these clouds (Webster and Stephens 1984) have a preferred phasing within the flow pattern in the middle latitudes. We would expect, for instance, that radiative heating of the upper troposphere near the large-scale ridge axis would transition to net cooling as the upstream inflection point is approached. GCMs must approximate these spatial relationships between cloud occurrence, cloud properties, and the resolved scale dynamics if the feedbacks by clouds are to be properly represented in climate simulations.

Acknowledgments. Primary funding for this work was supplied by the Environmental Science Division of the U.S. Department of Energy (Grant DE-FG0398ER62571) and by the NASA Radiation Science Program (Grant NNG04GF86G). Data were obtained from the Atmospheric Radiation Measurements Pro-

gram sponsored by the U.S. Department of Energy Office of Science, Office of Biological and Environmental Research, Environmental Science Division.

REFERENCES

Ackerman, T. P., and G. M. Stokes, 2003: The Atmospheric Radiation Measurement Program. *Phys. Today,* **56,** 38–45.

Brown, P. R., and P. N. Francis, 1995: Improved measurements of the ice water content in cirrus using a total-water probe. *J. Atmos. Oceanic Technol.,* **12,** 410–414.

Clothiaux, E. E., and Coauthors, 1999: The Atmospheric Radiation Measurement Program cloud radars: Operational modes. *J. Atmos. Oceanic Technol.,* **16,** 819–827.

——, T. P. Ackerman, G. G. Mace, K. P. Moran, R. T. Marchand, M. A. Miller, and B. E. Martner, 2000: Objective determination of cloud heights and radar reflectivities using a combination of active remote sensors at the ARM CART sites. *J. Appl. Meteor.,* **39,** 645–665.

Comstock, J. M., T. P. Ackerman, and G. G. Mace, 2002: Ground-based lidar and radar remote sensing of tropical cirrus clouds at Nauru Island: Cloud statistics and radiative impacts. *J. Geophys. Res.,* **107,** 4714, doi:10.1029/2002JD002203.

Del Genio, A. D., 2002: GCM simulation of cirrus for climate studies. *Cirrus,* D. K. Lynch et al., Eds., Oxford University Press, 310–326.

——, M.-S. Yao, W. Kovari, and K. K.-W. Lo, 1996: A prognostic cloud water parameterization for global climate models. *J. Climate,* **9,** 270–304.

Fu, Q., and K. N. Liou, 1993: Parameterization of the radiative properties of cirrus clouds. *J. Atmos. Sci.,* **50,** 2008–2025.

Gayet, J.-F., and Coauthors, 2004: Cirrus cloud microphysical and optical properties at southern and northern midlatitudes during the INCA experiment. *J. Geophys. Res.,* **109,** D20206, doi:10.1029/2004JD004803.

Heymsfield, A. J., 1977: Precipitation development in stratiform ice clouds. *J. Atmos. Sci.,* **34,** 367–381.

——, and L. J. Donner, 1990: A scheme for parameterizing ice-cloud water content in general circulation models. *J. Atmos. Sci.,* **47,** 1865–1877.

——, and G. M. McFarquhar, 2002: Mid-latitude and tropical cirrus: Microphysical properties. *Cirrus,* D. K. Lynch et al., Eds., Oxford University Press, 78–101.

Jensen, E., D. O.'C. Starr, and O. B. Toon, 2004: Mission investigates tropical cirrus clouds. *Eos, Trans. Amer. Geophys. Union,* **85,** 45–50.

Kalnay, E., and Coauthors, 1996: The NCEP/NCAR 40-Year Reanalysis Project. *Bull. Amer. Meteor. Soc.,* **77,** 437–471.

Khvorostyanov, V., and K. Sassen, 1998: Cirrus cloud simulation using explicit microphysics and radiation. Part II: Microphysics, vapor and ice mass budgets, and optical and radiative properties. *J. Atmos. Sci.,* **55,** 1822–1845.

Kistler, R., and Coauthors, 2001: The NCEP–NCAR 50-year reanalysis: Monthly means CD-ROM and documentation. *Bull. Amer. Meteor. Soc.,* **82,** 247–267.

Lin, R.-F., D. O.'C. Starr, J. Reichardt, and P. J. DeMott, 2005: Nucleation in synoptically forced cirrostratus. *J. Geophys. Res.,* **110,** D08208, doi:10.1029/2004JD005362.

Mace, G. G., D. O.'C. Starr, T. P. Ackerman, and P. Minnis, 1995: Examination of coupling between an upper tropospheric cloud system and synoptic scale dynamics diagnosed from wind profiler and radiosonde data. *J. Atmos. Sci.,* **52,** 4094–4127.

——, T. P. Ackerman, E. E. Clothiaux, and B. A. Albrecht, 1997: A study of composite cirrus morphology using data from a 94-GHz radar and correlations with temperature and large-scale vertical motion. *J. Geophys. Res.,* **102,** 13 581–13 593.

——, ——, P. Minnis, and D. F. Young, 1998: Cirrus layer microphysical properties derived from surface-based millimeter radar and infrared interferometer data. *J. Geophys. Res.,* **103,** 23 207–23 216.

——, E. E. Clothiaux, and T. P. Ackerman, 2001: The composite characteristics of cirrus clouds: Bulk properties revealed by one year of continuous cloud radar data. *J. Climate,* **14,** 2185–2203.

——, Y. Zhang, S. Platnick, M. D. King, P. Minnis, and P. Yang, 2005: Evaluation of cirrus cloud properties derived from MODIS radiances using cloud properties derived from ground-based data collected at the ARM SGP site. *J. Appl. Meteor.,* **44,** 221–240.

McGill, M. J., and Coauthors, 2004: Combined lidar-radar remotes sensing: Initial results from CRYSTAL-FACE. *J. Geophys. Res.,* **109,** D07203, doi:10.1029/2003JD004030.

Moran, K. P., B. E. Martner, M. J. Post, R. A. Kropfli, D. C. Welsh, and K. B. Widner, 1998: An unattended cloud-profiling radar for use in climate research. *Bull. Amer. Meteor. Soc.,* **79,** 443–455.

Platt, C. M. R., and A. C. Dilley, 1981: Remote sounding of high clouds. IV: Observed temperature variations in cirrus optical properties. *J. Atmos. Sci.,* **38,** 1069–1082.

Sassen, K., 2002: Cirrus: A modern perspective. *Cirrus,* D. K. Lynch et al., Eds., Oxford University Press, 11–40.

——, and G. C. Dodd, 1988: Homogeneous nucleation rate for highly supercooled cirrus cloud droplets. *J. Atmos. Sci.,* **45,** 1357–1369.

——, and J. R. Campbell, 2001: A midlatitude cirrus cloud climatology from the Facility for Atmospheric Remote Sensing. Part I: Macrophysical and synoptic properties. *J. Atmos. Sci.,* **58,** 481–496.

——, and J. M. Comstock, 2001: A midlatitude cirrus cloud climatology from the Facility for Atmospheric Remote Sensing. Part III: Radiative properties. *J. Atmos. Sci.,* **58,** 2113–2127.

——, D. O.'C. Starr, and T. Uttal, 1989: Mesoscale and microscale structure of cirrus clouds: Three case studies. *J. Atmos. Sci.,* **46,** 371–386.

——, W. P. Arnott, D. O.'C. Starr, G. G. Mace, Z. Wang, and M. R. Poellot, 2003: Midlatitude cirrus clouds derived from Hurricane Nora: A case study with implications for ice crystal nucleation and shape. *J. Atmos. Sci.,* **60,** 873–891.

Smith, G. L., B. R. Barkstrom, E. F. Harrison, R. B. Lee III, and B. A. Wielicki, 1994: Radiation budget measurements for the eighties and nineties. *Adv. Space Res.,* **14,** 81–84.

Smith, W. L., X. L. Ma, S. A. Ackerman, H. E. Revercomb, and R. O. Knuteson, 1993: Remote sensing cloud properties from high spectral resolution infrared observations. *J. Atmos. Sci.,* **50,** 1708–1720.

Spatz, C., 1997: *Basic Statistics: Tales of Distributions*. Brooks/Cole Publishing, 488 pp.

Starr, D. O.'C., 1987: Effects of radiative processes in thin cirrus. *J. Geophys. Res.,* **92,** 3973–3978.

——, and S. K. Cox, 1985: Cirrus clouds. Part II: Numerical experiments on the formation and maintenance of cirrus. *J. Atmos. Sci.,* **42,** 2682–2694.

——, and D. P. Wylie, 1990: The 27–28 October 1986 FIRE IFO

cirrus case study: Meteorology and clouds. *Mon. Wea. Rev.,* **118,** 2259–2287.

Stephens, G. L., 2005: Cloud feedback in the climate system: A critical review. *J. Climate,* **18,** 237–273.

Stubenrauch, C. J., F. Eddounia, and G. Radel, 2004: Correlations between microphysical properties of large-scale semi-transparent cirrus and the state of the atmosphere. *Atmos. Res.,* **72,** 403–423.

Sundqvist, H., 2002: On cirrus modeling for general circulation and climate models. *Cirrus,* D. K. Lynch et al., Eds., Oxford University Press, 297–309.

Webster, P. J., and G. L. Stephens, 1984: Cloud–radiation interaction and the climate problem. *The Global Climate*, J. Houghton, Ed., Cambridge University Press, 63–78.

Wielicki, B., 2001: New generation of CERES radiation budget data available. *Earth Obs.,* **13,** 23–24.

Wylie, D. P., and W. P. Menzel, 1999: Eight years of high cloud statistics using HIRS. *J. Climate,* **12,** 170–184.